Analysis of optical waveguide structures by use of a combined finite-difference/ finite-difference time-domain method

Jon W. Wallace and Michael A. Jensen

Department of Electrical and Computer Engineering, 459 Clyde Building, Brigham Young University, Provo, Utah 84602

Received May 4, 2001; revised manuscript received August 7, 2001; accepted August 7, 2001

We present a method for full-wave characterization of optical waveguide structures. The method computes mode-propagation constants and cross-sectional field profiles from a straightforward discretization of Maxwell's equations. These modes are directly excited in a three-dimensional finite-difference time-domain simulation to obtain optical field transmission and reflection coefficients for arbitrary waveguide discontinuities. The implementation uses the perfectly-matched-layer technique to absorb both guided modes and radiated fields. A scattered-field formulation is also utilized to allow accurate determination of weak scattered-field strengths. Individual three-dimensional waveguide sections are cascaded by S-parameter analysis. A complete 10^4-section Bragg resonator is successfully simulated with the method. © 2002 Optical Society of America

OCIS codes: 000.3860, 000.4430, 060.2310, 230.1480, 230.7370.

1. INTRODUCTION

The ability to design complex optical devices is greatly enhanced by simulation tools that characterize wave propagation in arbitrary guiding structures. Complete electromagnetic characterization of such geometries requires two basic tools: (1) a two-dimensional simulation technique capable of finding propagation constants and mode profiles for arbitrary guiding structures, and (2), a three-dimensional (3D) electromagnetic analysis method to simulate mode propagation in the presence of waveguide transitions and discontinuities. For electrically large structures, limited computer memory and processing power often preclude a complete full-wave 3D analysis. In many cases, however, simulation efficiency can be greatly enhanced through appropriate application of network analysis.

Prior work in this area has focused on two-dimensional planar waveguide approximations,[1,2] the approximate beam-propagation method,[3,4] and finite-difference (FD) solutions for propagation constants and mode profiles.[5,6] In this paper we employ a simple FD method based on a straightforward discretization of Maxwell's equations to determine mode characteristics for waveguides of arbitrary cross-sectional geometry. The equations may be solved using sparse eigenvalue/eigenvector methods or iteratively by using a sparse linear-equation solver. These modes are used in a full-wave analysis of 3D structures with the finite-difference time-domain (FDTD) method[7,8] with Berenger's perfectly-matched-layer (PML) absorbing boundary condition.[9] To characterize optically large waveguide devices, S-parameter analysis is employed to combine the response of individual 3D sections.

We demonstrate the three-step method by analyzing an electrically large buried heterostructure Bragg resonator employing a surface relief grating. The ability of the method to provide realistic results for this numerically sensitive problem provides evidence that the method may be applied to a wide variety of structures.

2. FINITE-DIFFERENCE MODE SOLUTION

Finite-difference methods based on discretizations of the time-harmonic Helmholtz equation have been successfully applied for vectorial-mode extraction.[5] However, such methods often require special treatment of material boundaries, and the mode solutions obtained often deviate slightly from modes supported by other discretizations (FDTD, for example). Full vectorial-mode solutions have also been demonstrated by applying a Fourier transform to the FD-vector beam propagation method.[6]

Here we employ a straightforward discretization of the time-harmonic form of Maxwell's equations, using Yee's discretization scheme. An obvious advantage is natural compatibility with subsequent 3D FDTD simulations. The method is free of spurious modes since the FDTD gridding scheme automatically satisfies Maxwell's divergence relations. Also, if material parameters are specified for each FDTD cell, the gridding arrangement ensures satisfaction of appropriate field continuity conditions across material boundaries.

A. Discretization of Maxwell's Equations

Assuming $\exp(j\omega t)$ time variation and $\exp(-j\beta_z z)$ longitudinal spatial variation for a propagating mode, we may write Maxwell's equations for a nonmagnetic medium as

$$H_x = \frac{1}{k_0}\left(j\frac{\partial E_z}{\partial y} - \beta_z E_y\right),$$

$$E_x = \frac{1}{\epsilon_r k_0}\left(\beta_z H_y - j\frac{\partial H_z}{\partial y}\right),$$

$$H_y = \frac{1}{k_0}\left(\beta_z E_x - j\frac{\partial E_z}{\partial x}\right),$$

$$E_y = \frac{1}{\epsilon_r k_0}\left(j\frac{\partial H_z}{\partial x} - \beta_z H_x\right),$$

$$H_z = \frac{j}{k_0}\left(\frac{\partial E_y}{\partial x} - \frac{\partial E_x}{\partial y}\right), \qquad E_z = \frac{j}{\epsilon_r k_0}\left(\frac{\partial H_x}{\partial y} - \frac{\partial H_y}{\partial x}\right), \tag{1}$$

where E denotes electric-field intensity, H represents magnetic-field intensity multiplied by the free-space intrinsic impedance η_0, and the subscripts $\{x,y,z\}$ denote field polarization. Also, $k_0 = \omega\sqrt{\mu_0\epsilon_0}$ is the free-space wave number and ϵ_r is the material relative permittivity. To discretize these equations, we use the standard Yee grid assignment[8] collapsed onto a two-dimensional surface as shown in Fig. 1. After applying first-order central differences we obtain

$$H_{x,ij} = \frac{1}{k_0}\left(j\frac{E_{z,\,ij} - E_{z,\,i,\,j-1}}{\Delta y} - \beta_z E_{y,\,ij}\right),$$

$$H_{y,ij} = \frac{1}{k_0}\left(\beta_z E_{x,\,ij} - j\frac{E_{z,\,ij} - E_{z,\,i-1,\,j}}{\Delta x}\right),$$

$$jH_{z,ij} = \frac{1}{k_0}\left(\frac{E_{x,\,ij} - E_{x,\,i,\,j-1}}{\Delta y} - \frac{E_{y,\,ij} - E_{y,\,i-1,\,j}}{\Delta x}\right),$$

$$E_{x,ij} = \frac{1}{\epsilon_r k_0}\left(\beta_z H_{y,\,ij} - j\frac{H_{z,\,i,\,j+1} - H_{z,\,ij}}{\Delta y}\right),$$

$$E_{y,ij} = \frac{1}{\epsilon_r k_0}\left(j\frac{H_{z,\,i+1,\,j} - H_{z,\,ij}}{\Delta x} - \beta_z H_{x,\,ij}\right),$$

$$jE_{z,ij} = \frac{1}{\epsilon_r k_0}\left(\frac{H_{y,\,i+1,\,j} - H_{y,\,ij}}{\Delta x} - \frac{H_{x,\,i,\,j+1} - H_{x,\,ij}}{\Delta y}\right), \tag{2}$$

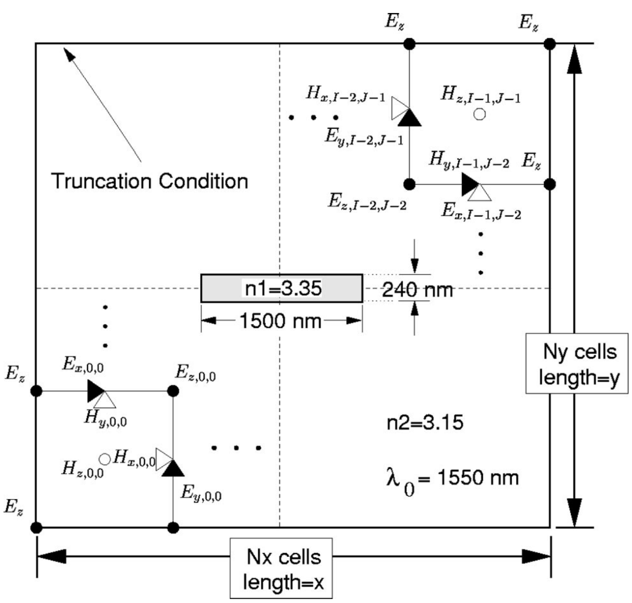

Fig. 1. Waveguide geometry used to assess error in the propagation constant and field profile found with the FD method. Also shown is the assignment of FD grid indices.

where ϵ_r now represents the relative permittivity averaged over one cell centered about the component on the left-hand side in each equation.

B. Boundary Truncation Conditions

The FD method requires a truncation condition for the field components at the outer domain boundary. Simple Neumann or Dirichlet conditions are often employed. However, such nonphysical boundaries may induce unacceptable error when placed near the guiding structure. To develop an approach that more closely matches the true field behavior, we note that for a cylindrical waveguide the field profile for the HE_{11} mode decays outside of the core as $H_1^{(1)}(j\alpha\rho)$, where $\alpha = (\beta_z^2 - \omega^2\mu_1\epsilon_1)^{1/2}$. For $\alpha\rho > 2$, the function is approximately $(1/\sqrt{\rho})\exp(-\alpha\rho)$, which provides an approximate functional relationship between fields that lie on the boundary and those just inside the boundary. As shown in Subsection 2.E, use of this boundary condition significantly reduces the required size of the computational grid for a given level of accuracy. Similar localized boundary conditions have been employed in the finite-element method for open-boundary waveguides.[10]

C. Iterative Linear Method

One approach to solving Eq. (2) is to construct a vector of field components to obtain the matrix equation $\mathbf{Af} = \mathbf{f}_0$, where $\mathbf{f} = [\{H_{x,ij}\}\{H_{y,ij}\}\{jH_{z,ij}\}\{E_{x,ij}\}\{E_{y,ij}\}\{jE_{z,ij}\}]^T$ and $\{\cdot\}$ represents a stacking operation. Solving this equation using matrix inversion requires that the forcing vector $\mathbf{f}_0$ be nonzero and β_z be fixed. We can make the forcing vector nonzero by fixing one of the field components at a specific node. We then find the value of β_z that minimizes the vector norm $\|\mathbf{A}'(\beta_z)\mathbf{f}\|$, where $\mathbf{A}'$ is the coefficient matrix obtained when no forcing is in effect. The minimization is performed by optimization after specifying an initial guess for β_z from an approximate analytical solution or using the eigenvalue/eigenvector method outlined in Subsection 2.D.

The simulations were performed on a 700-MHz Pentium-based PC with 512 megabytes of memory. The SuperLU package was used to compute sparse linear matrix equation solutions. For a 60×120 FD grid, each iteration required 15 s. Approximately 100 iterations were required to obtain 10^{-9} accuracy in the propagation constant.

D. Eigenvalue/Eigenvector Method

Substituting the expressions for jH_z and jE_z in Eq. (2) into the remaining four equations and rearranging those equations produces the relations

Table 1. Propagation Constant Value and Fractional Error for Various Sizes of the Simulation Domain

Cells		Size (nm)		Zero Bound		Decay Bound	
N_x	N_y	x	y	$\beta_z\lambda_0$	Fractional Error	$\beta_z\lambda_0$	Fractional Error
36	48	2700	2880	19.96636646	2.37×10^{-4}	19.96168858	2.51×10^{-6}
48	64	3600	3840	19.96267660	5.20×10^{-5}	19.96164637	3.96×10^{-7}
60	80	4500	4800	19.96186515	1.13×10^{-5}	19.96163969	6.08×10^{-8}
72	96	5400	5760	19.96168746	2.43×10^{-6}	19.96163867	9.63×10^{-9}
84	112	6300	6720	19.96164903	5.04×10^{-7}	19.96163851	1.55×10^{-9}
96	128	7200	7680	19.96164075	8.94×10^{-8}	19.96163848	2.26×10^{-10}
108	144	8100	8640	19.96163896	0.00×10^{0}	19.96163847	0.00×10^{0}

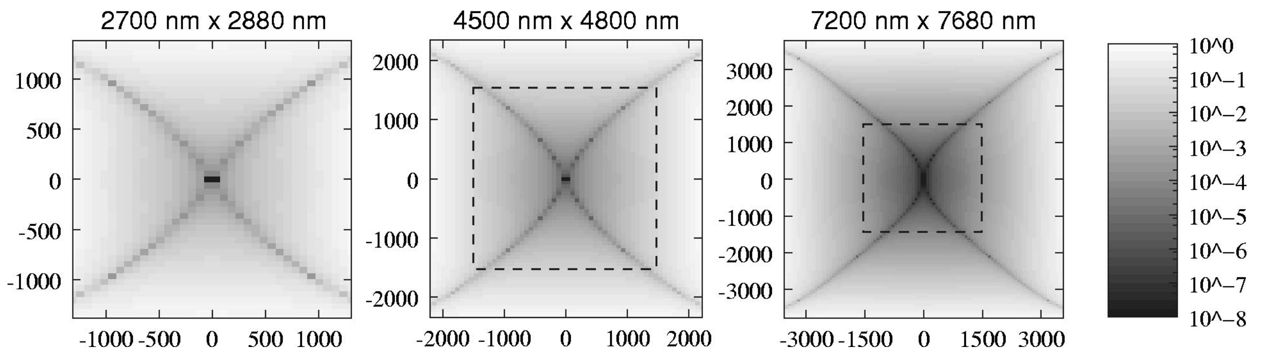

Fig. 2. Error in the mode E_x field profile for the zero-field boundary condition. The dashed line gives the dimensions of the smallest domain for comparison.

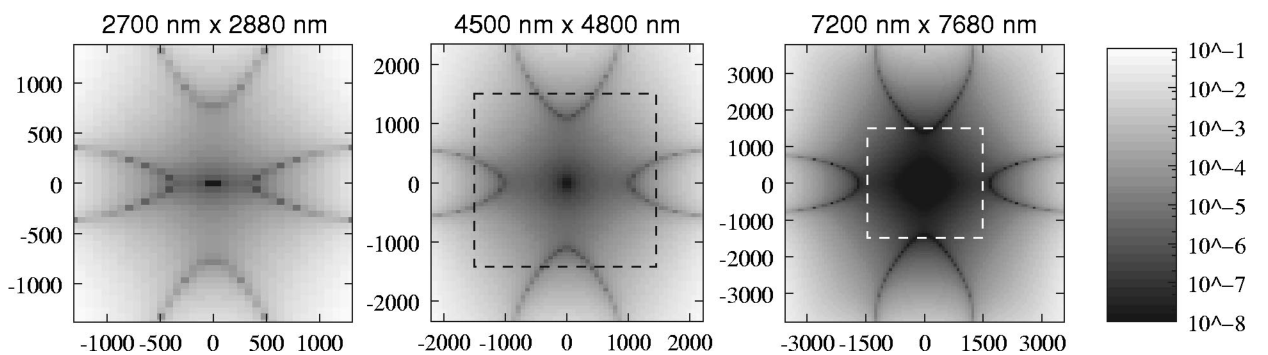

Fig. 3. Error in the mode E_x field profile for the decay boundary condition. The dashed line gives the dimensions of the smallest domain for comparison.

$$\beta_z E_{x,\,ij} = \frac{1}{k_0 \Delta x}\left(\frac{H_{y,i+1,j}}{\epsilon^z_{r,ij}\Delta x} - \frac{H_{x,i,j+1} - H_{x,ij}}{\epsilon^z_{r,ij}\Delta y} + \frac{H_{y,i-1,j}}{\epsilon^z_{r,i-1,j}\Delta x} + \frac{H_{x,i-1,j+1} - H_{x,i-1,j}}{\epsilon^z_{r,i-1,j}\Delta y}\right) + \left[k_0 - \frac{1}{k_0(\Delta x)^2}\left(\frac{1}{\epsilon^z_{r,ij}} + \frac{1}{\epsilon^z_{r,i-1,j}}\right)\right] H_{y,ij}\,,$$

$$\beta_z E_{y,\,ij} = \frac{1}{k_0 \Delta y}\left(\frac{H_{y,i+1,j} - H_{y,ij}}{\epsilon^z_{r,ij}\Delta x} - \frac{H_{x,i,j+1}}{\epsilon^z_{r,ij}\Delta y} - \frac{H_{y,i+1,j-1} - H_{y,i,j-1}}{\epsilon^z_{r,i,j-1}\Delta x} - \frac{H_{x,i,j-1}}{\epsilon^z_{r,i,j-1}\Delta y}\right) + \left[\frac{1}{k_0(\Delta y)^2}\left(\frac{1}{\epsilon^z_{r,ij}} + \frac{1}{\epsilon^z_{r,i,j-1}}\right) - k_0\right] H_{x,ij}\,,$$

$$\beta_z H_{x,\,ij} = \frac{1}{k_0 \Delta x}\left(\frac{E_{x,i+1,j} - E_{x,i+1,j-1} - E_{x,ij} + E_{x,i,j-1}}{\Delta y} - \frac{E_{y,i+1,j} + E_{y,i-1,j}}{\Delta x}\right) + \left[\frac{2}{k_0(\Delta x)^2} - \epsilon^y_{r,ij} k_0\right] E_{y,ij}\,,$$

$$\beta_z H_{y,\,ij} = \frac{1}{k_0 \Delta y}\left(\frac{E_{x,i,j+1} + E_{x,i,j-1}}{\Delta y} + \frac{E_{y,i-1,j+1} - E_{y,i,j+1} + E_{y,ij} - E_{y,i-1,j}}{\Delta x}\right) + \left[\epsilon^x_{r,ij} k_0 - \frac{2}{k_0(\Delta y)^2}\right] E_{x,ij}\,, \tag{3}$$

where $\epsilon_{r,ij}^{\{x,y,z\}}$ represents the relative permittivity averaged about the $E_{x,ij}$, $E_{y,ij}$, or $E_{z,ij}$ component, respectively. For small cell sizes, the terms containing $(\Delta x)^2$ and $(\Delta y)^2$ lead to coefficient matrices that have poor numerical conditioning and consequently sparse eigenvalue solvers such as ARPACK have difficulty converging. For fine detail, the eigenvalue method may be used on a coarse grid to obtain an initial guess for β_z that subsequently may be refined with the linear method. This approach is presented in Ref. 11 for a cylindrical waveguide. In this paper, initial guesses for propagation constants were computed on a 30×60 FD grid using ARPACK, requiring approximately one minute of computation.

E. Accuracy of the Mode Solution

In this section the linear solution method is applied to a rectangular dielectric waveguide whose cross section matches the core of the Bragg resonator that will be analyzed in Subsection 2.F. Here, we assess the accuracy of the propagation constant and field shape for the propagating mode with respect to boundary-truncation type, domain size, and cell size. The basic geometry to be simulated is depicted in Fig. 1. Note that error in this section is quantified as the fractional deviation from the most accurate numerical solution obtained (largest-size domain/finest resolution).

1. Domain Size Dependence

Table 1 compares the fractional error in the propagation constant for various grid sizes with the zero-field boundary and decay boundary. The cell size is held constant for all computations. Figures 2 and 3 plot the error in the E_x-field component for the zero and the decay boundary conditions, respectively. This comparison shows that the error produced by the decay condition is an order of magnitude lower than that produced by the zero-truncation condition. The results also indicate that a modest domain size ($4500\ \mathrm{nm} \times 4800\ \mathrm{nm}$) gives reasonably small error in the propagation constant (10^{-7}) and field profile (10^{-3}). For all further computations, the decay-truncation approach will be used.

2. Cell Size Dependence

Table 2 lists the fractional error in the propagation constant for various cell sizes when the domain size is held constant. These values show that the propagation constant is more sensitive to the discretization than to the domain size. Figure 4 shows the error in the E_x component of the computed field profile for three of the cases considered.

F. Bragg-Resonator Guided-Mode Solution

Figure 5 shows the Bragg-resonator geometry under consideration. This geometry is based on the buried heterostructure distributed feedback device cross section given in Ref. 12 with parameters specified at a physical temperature of $T = 25\,°\mathrm{C}$ and a wavelength of $\lambda = 1.55\ \mu\mathrm{m}$. The index of refraction[13,14] for the cladding (InP) at this temperature is $n_2 = 3.15$. The core ($\mathrm{Ga}_{1-x}\mathrm{In}_x\mathrm{As}_y\mathrm{P}_{1-y}$) is assumed to be matched to the InP lattice with $x = 0.2$ and $y = 0.43$, giving $n_1 = 3.35$ (Ref. 15).

The refractive index in the grating (n_3) is a function of longitudinal position. For the true physical geometry, the grating would have $n_3 = n_1 = 3.35$ and the height would be modulated (surface relief). However, modeling such fine detail significantly increases the memory required for simulation. Instead, we use alternate values for n_3 of 3.35 and 3.33 for our grating modulation, which corresponds to a 10% modulation in the grating height when viewed in terms of an effective permittivity of the grating. Mode solutions are required only in the unmodulated region ($n_3 = 3.35$).

The propagation constants and modal field profiles were computed at six different wavelengths by using the iterative linear method to refine the solution from the eigenvalue/eigenvector method. The wavelengths and propagation constants are given in Table 3. FDTD simulations required approximately 2 h to simulate 10 periods of modal oscillation.

3. THREE-DIMENSIONAL SIMULATIONS OF BRAGG-RESONATOR SECTION

The Bragg resonator can be divided into sections, each having the geometry depicted in Fig. 6. The section

Table 2. Propagation Constant Value and Error for Various Simulation Cell Sizes

N_x	N_y	x	y	$\beta_z\lambda_0$	Fractional Error
30	40	4500	4800	19.95706883	-2.94×10^{-4}
60	80	4500	4800	19.96163969	-6.47×10^{-5}
90	120	4500	4800	19.96245221	-2.40×10^{-5}
120	160	4500	4800	19.96273238	-9.92×10^{-6}
150	200	4500	4800	19.96286096	-3.48×10^{-6}
180	240	4500	4800	19.96293039	0.00×10^{0}

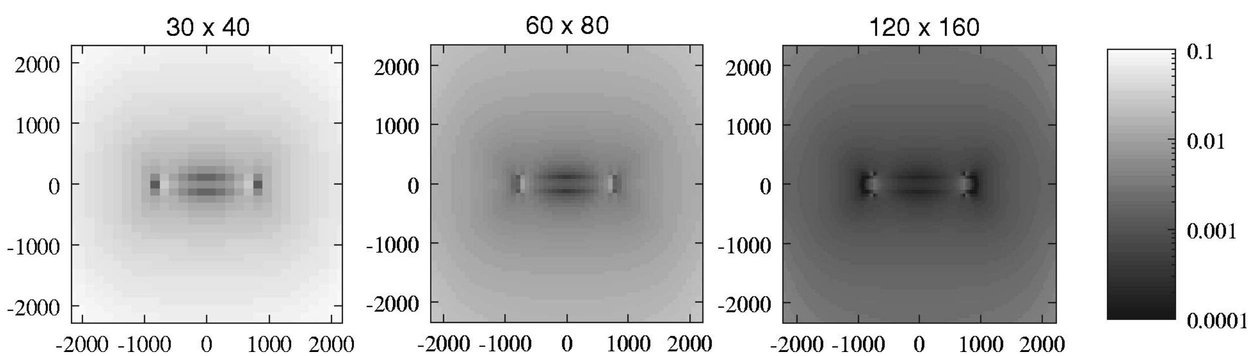

Fig. 4. Error in the mode E_x field profile for the decay boundary condition for various grid resolutions.

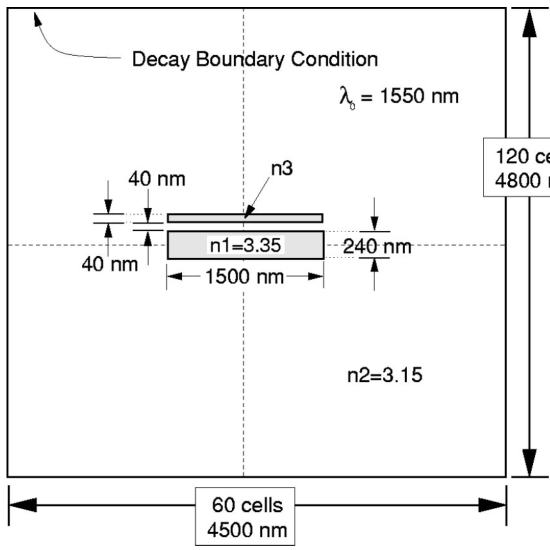

Fig. 5. Waveguide cross section for the Bragg resonator. n_3 takes on discrete values in the longitudinal direction.

length of 120 nm was chosen since it is approximately λ/4 for the guided mode.

FDTD[7,8] was chosen for simulating the 3D Bragg resonator because of its computational efficiency and ease of implementation. FDTD is generally well suited for free-space propagation and scattering problems. When applied to the Bragg resonator, important considerations include the following:

1. Wideband excitation may not be possible owing to wavelength-dependent mode profiles and propagation constants.
2. Discrete stepping in time and finite resolution in the propagation direction will lead to a mode slightly different from that given by Eq. (2), where exact derivatives have been assumed in time and propagation direction.
3. The fields scattered by the 3D geometry will be very weak compared to the incident wave, giving rise to large dynamic range requirements.
4. The error induced by the absorbing boundary condition must be acceptably low. This is particularly important, as the Bragg-resonator frequency response can be highly sensitive to errors in the computed fields.

A. Wideband and Sinusoidal Excitation

By employing an appropriate time-domain waveform, FDTD can obtain the wideband response of many important structures with a single simulation. Since mode profiles and propagation constants will change as a function of excitation wavelength, wideband excitation is not well suited for applications that are very sensitive to error. Thus in this paper separate simulations were run at discrete wavelengths to obtain the transmission and reflection of the Bragg section, and interpolation was applied to obtain results at intermediate wavelengths. Subsection 3.C explains how the guided mode at a single wavelength is sourced in an FDTD simulation.

B. Finite-Difference Approximation

FDTD approximates continuous derivatives in time and space with finite differences. In Eqs. (2) and (3), continuous derivatives are assumed in z and time. To ensure complete compatibility of the mode shape, we must solve Eq. (1) with finite differences in time and space.

Assuming time-harmonic fields, the finite difference (D_t) of any field quantity (F) with respect to time is $D_t[F(x, y, z)\exp(j\omega n\Delta t)] = j\omega\,\mathrm{sinc}(\omega\Delta t/2)\quad F(x, y, z) \times \exp(j\omega n\Delta t)$, where $\mathrm{sinc}(x) = \sin(x)/x$. Thus k_0 in Eq. (2) must be replaced with $k_0\,\mathrm{sinc}(\omega\Delta t/2)$. Similarly, application of finite differences in the propagation direction requires replacement of β_z with $\beta_z\,\mathrm{sinc}(\beta_z\Delta z/2)$. These replacements will be used in Subsection 4.B to assess the accuracy of the complete Bragg solution.

C. Dynamic Range: Scattered-Field Formulation for Waveguides

For many waveguide geometries, such as a small section of a Bragg resonator, the field scattered by the obstacle may be significantly weaker than the incident field. In these situations, finite precision arithmetic may produce unacceptable error levels.

To minimize the dynamic range requirements as well as remove the need to absorb the strong incident field at the domain boundaries, we utilize the scattered-field formulation in the FDTD implementation.[8] This approach, which has been used extensively to model electromagnetic scattering in free space, can also be applied to waveguide analysis. In this case, however, the incident field and corresponding geometry are the incident mode and the unperturbed waveguide structure, respectively, where the waveguide material parameters are represented by ϵ_i, μ_i, and σ_i. If the actual (perturbed) waveguide geometry is characterized by material parameters ϵ, μ, and σ, we may write Maxwell's equations for the scattered fields ($\bar{E}_s$ and $\bar{H}_s$) as

$$\nabla \times \bar{E}_s = -\mu \frac{\partial \bar{H}_s}{\partial t} - (\mu - \mu_i)\frac{\partial \bar{H}^{\mathrm{inc}}}{\partial t}, \tag{4}$$

$$\nabla \times \bar{H}_s = \epsilon \frac{\partial \bar{E}_s}{\partial t} + \sigma \bar{E}_s + (\epsilon - \epsilon_i)\frac{\partial \bar{E}^{\mathrm{inc}}}{\partial t} + (\sigma - \sigma_i)\bar{E}^{\mathrm{inc}}, \tag{5}$$

where $\bar{E}^{\mathrm{inc}}$ and $\bar{H}^{\mathrm{inc}}$ represent the incident modal fields. These equations are identical to Maxwell's equations for total field with the addition of source terms. For a nonconductive, nonmagnetic medium, we must include a source term only where $\epsilon \neq \epsilon_i$. To illustrate the excitation of the source in the FDTD code, the standard FDTD update equation for E_x is given as

$$E_{x,ijk}^{n+1/2} = \frac{\Delta t}{\epsilon}\left(\frac{H_{z,i,j+1/2,k}^{n} - H_{z,i,j-1/2,k}}{\Delta y} - \frac{H_{y,i,j,k+1/2}^{n} - H_{y,i,j,k-1/2}}{\Delta z}\right) + E_{x,ijk}^{n-1/2} \tag{6}$$

$$\equiv \mathcal{G}. \tag{7}$$

Table 3. Propagation Constants and Transmission and Reflection Coefficients for the Bragg Section at Various Wavelengths

λ_0 (nm)	$\beta_z \lambda_0$	$\lvert R_0 \rvert$	$\angle R_0$ (deg)	$\lvert T_{0,0} - 1 \rvert$	$\angle(T_{0,0} - 1)$ (deg)
1549.0	20.009476	2.7232×10^{-4}	1.27	4.2981×10^{-4}	90.0379
1549.5	20.009300	2.7222×10^{-4}	1.30	4.2952×10^{-4}	90.0375
1550.0	20.009125	2.7212×10^{-4}	1.33	4.2922×10^{-4}	90.0372
1550.5	20.008949	2.7202×10^{-4}	1.36	4.2893×10^{-4}	90.0368
1551.0	20.008774	2.7192×10^{-4}	1.39	4.2864×10^{-4}	90.0364
1551.5	20.008599	2.7182×10^{-4}	1.42	4.2834×10^{-4}	90.0360

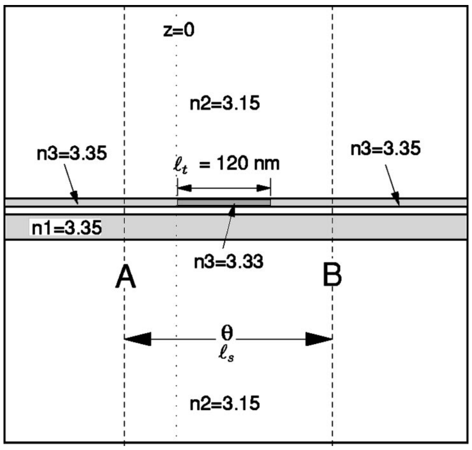

Fig. 6. Section of the Bragg resonator to be modeled with 3D full-wave analysis. The dashed lines denote the extents of the unit section, l_t and l_s are physical lengths of the tooth and Bragg section, and θ is the angular length of the section in radians at $\lambda_0 = 1550$ nm.

The incident/scattered field formulation introduces an additional term such that

$$E_{x,ijk}^{n+1/2} = \mathcal{G} + \frac{(\epsilon_i - \epsilon)}{\epsilon} \Delta t \left. \frac{\partial E_{x,ijk}^{\text{inc}}}{\partial t} \right|_{t=n\Delta t} \tag{8}$$

$$= \mathcal{G} + \frac{(\epsilon_i - \epsilon)}{\epsilon} (E_{x,ijk}^{\text{inc},\, n+1/2} - E_{x,ijk}^{\text{inc},\, n-1/2}), \tag{9}$$

where E^{inc} is specified by the known mode shape. The second equality employs a finite difference on the incident source to ensure compatibility of the mode in the discretized domain. After the FDTD simulation, scattered fields may be converted to physical total fields by adding the known incident mode shape at each simulation node.

D. Absorbing Boundary Condition: Berenger's Perfectly Matched Layer for Waveguides

Several absorbing boundary conditions have been applied for waveguide termination: methods based on the one-way wave equation,[16,17] PML techniques,[9,18,19] modal eigenfunction expansion approaches,[20] absorption based on discrete time-domain Green's functions for the waveguide,[21,22] and filter-bank methods.[23] Our problem requires absorption of both guided modes and radiated fields, suggesting the use of robust PML-based methods. Berenger's PML[9] is well suited for free-space scattering problems. To apply the method to waveguide simulation, two different issues must be considered.

1. *Propagation into the Perfectly Matched Layer*

Past work has demonstrated that the PML technique may be applied to a dielectric waveguide by simply extending the waveguide into the PML and ensuring that $\sigma_{1,z}(z)/\sigma_{2,z}(z) = \epsilon_1/\epsilon_2$, where $\sigma_{1,z}(z)$ and $\sigma_{2,z}(z)$ are the z-directed conductivities in the PML for the core and cladding and ϵ_1 and ϵ_2 are the permittivities in core and cladding, respectively.[24] This condition ensures that the decay rate of the propagating mode in the core and cladding remains equal. Many other researchers have studied Maxwell's equations in the PML.[18,19,25]

Here, we provide a proof suited for our application that if the waveguide naturally extends into the PML, the modes are identical in the PML and normal regions, leading to a (theoretically) reflectionless interface. Note that matching of modes does not guarantee absorption. In the case of metallic waveguides, for example, we have the difficulty of evanescent modes, and other methods must be employed.

Starting with Berenger's equations for the PML in continuous space, assuming steady-state fields, and substituting equations for electric field into equations for magnetic field leads to the Helmholtz equation

$$\left(a_x b_x \frac{\partial^2}{\partial x^2} + a_y b_y \frac{\partial^2}{\partial y^2} + a_z b_z \frac{\partial^2}{\partial z^2} - 1 \right) H_p$$

$$= b_p \frac{\partial}{\partial p} \left(a_x \frac{\partial H_x}{\partial x} + a_y \frac{\partial H_y}{\partial y} + a_z \frac{\partial H_z}{\partial z} \right), \tag{10}$$

where $a_p = 1/(j\omega\mu + \sigma_p^*)$, $b_p = 1/(j\omega\epsilon + \sigma_p)$, and $p \in \{x, y, z\}$. A similar relation results for E when the substitution is performed in reverse. The right-hand side of Eq. (10) is identically 0 when the FDTD gridding scheme is used. In this case, for a PML only in the propagation direction, we obtain

$$\frac{1}{\omega^2 \mu \epsilon} \left(\frac{\partial \psi^2}{\partial x^2} + \frac{\partial \psi^2}{\partial y^2} + \frac{1}{\mu_{zr} \epsilon_{zr}} \frac{\partial \psi^2}{\partial z^2} \right) + \psi = 0, \tag{11}$$

where $\mu_{zr} = [1 - j\sigma_z^*/(\omega\mu)]$, $\epsilon_{zr} = [1 - j\sigma_z/(\omega\epsilon)]$, and ψ is any field quantity. Assuming the same condition as Berenger for a reflectionless interface, we let $q_z = \mu_{zr} = \epsilon_{zr}$. Modal propagation will be of the form $\psi = \psi(x, y)\exp(-j\beta_z' z)$ where $\beta_z' = \beta_z \sqrt{\mu_{zr}\epsilon_{zr}} = \beta_z q_z$. Substitution into Eq. (11) gives the Helmholtz equation

$$\left(\frac{\partial^2}{\partial x^2} + \frac{\partial^2}{\partial y^2} - \beta_z^2 + \omega^2 \mu \epsilon\right)\psi(x, y) = 0. \qquad (12)$$

Thus the governing equation for propagation constants does not change across the normal/PML or PML/PML interfaces.

To show that the mode shape is also continuous across the boundary, we write Faraday's law in the PML medium as

$$-j\omega\mu \bar{H}(x, y)\exp(-j\beta_z' z) = [\nabla_T \times \bar{E}(x, y)]\exp(-j\beta_z' z) + \left(\frac{1}{q_z}\frac{\partial}{\partial z}\hat{z}\right) \times [\bar{E}(x, y)\exp(-j\beta_z' z)]$$

$$-j\omega\mu \bar{H}(x, y) = [\nabla_T \times \bar{E}(x, y)] - \frac{\beta_z q_z}{q_z}[\hat{z} \times \bar{E}(x, y)], \quad (13)$$

where $\nabla_T \times$ represents the transverse part of the curl operator ($\nabla_T = [\partial/\partial x]\hat{x} + [\partial/\partial y]\hat{y}$), and $\times$ is the cross-product operator. Canceling the q_z terms leads to the same equation as in the non-PML medium. Repeating this analysis for Ampere's law shows that the equations for the cross-sectional mode shape are identical in the PML and normal regions.

When applying the PML, a stepped n-order conductivity gradient is convenient, or $\sigma(z) = \sigma_{\max}(z/\Delta z)^n$, where $\sigma_{\max}$ is the maximum conductivity and Δz is the length of the PML. The decay rate at any point in the PML is $\kappa(z) = \mathrm{Im}\{\beta_z[1 - j\sigma(z)/(\omega\epsilon)]\}$, and the accompanying reflection for the complete PML is $R = \exp\{(-2\sigma_{\max}\beta_z\Delta z)/[\omega\epsilon(n + 1)]\}$. To determine the conductivity in our FDTD simulation we compute

$$\frac{\sigma_{\max}}{\epsilon_r} = -\frac{(n + 1)\ln R\,\epsilon_0\omega}{2\beta_z\Delta z}, \qquad (14)$$

where R is the specified modal reflection. For each region of different ϵ_r in the waveguide cross section, we will have a different $\sigma_{\max}$ according to Eq. (14). This condition is equivalent to that given in Ref. 24.

2. Transverse Perfectly Matched Layer

In order to absorb fields radiated from waveguide discontinuities, we place the PML on the transverse sides ($\hat{x}$ and $\hat{y}$) of the simulation volume. The Helmholtz equation will not be the same in the normal and PML regions, leading to aberrations in the mode shape. However, if the field is weak in the PML region, we expect the effect to be small. To show this, consider the FDTD simulation volume depicted in Fig. 7. The Bragg-resonator waveguide geometry is the same as that shown in Fig. 5. The source for the simulations is an electric wall at the left side of the volume that is forced to the known mode. A ramp function of Gaussian shape and 99% rise time of $3T$ (3 periods) is applied to avoid initial transients. The steady-state fields are extracted by taking the fast Fourier transform (FFT) of a complete period after $10T$ and using the sample corresponding to the fundamental frequency. The results of these simulations have been compared with the solution given by an ideal one-dimensional (1D) FD simulation, where discretization applies only in the $\hat{z}$ direction. The decay boundary condition is used in the FD solver on the transverse walls in order to ensure compatibility of the guided mode.

The results of the computations using the 1D and FDTD solutions were compared in terms of complex-field envelopes at the center of the simulation (on the line $x = 0, y = 0$) and on complex-mode envelopes using Eq. (15). The fractional difference between the ideal 1D solution and the FDTD solution was below 5×10^{-6} and 1.5×10^{-5} for the simulations with no transverse PML and simulations with transverse PML, respectively. These results indicate that the PML at the domain edges influences negligible error on the mode behavior.

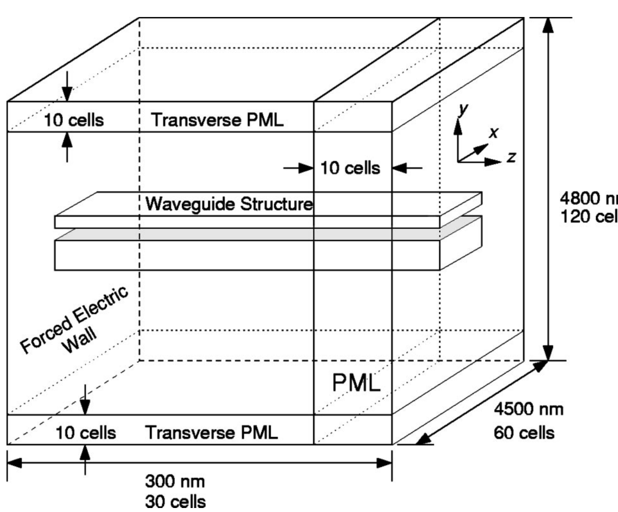

Fig. 7. FDTD simulation volume used to assess performance of propagation and transverse PML.

E. Mode Extraction

Because of mode orthogonality, the complex envelope of the mode with shape M_{ij} can be extracted from the fundamental frequency component of the FDTD simulation $E_{ij,z}$ by using the expression

$$A_z = \frac{\Sigma_{ij} E_{ij,z} M_{ij}^*}{\Sigma_{ij}|M_{ij}|^2}. \qquad (15)$$

4. BRAGG-RESONATOR RESPONSE

FDTD simulations were run for the wavelengths given in Table 3 by using simulation volume dimensions nearly

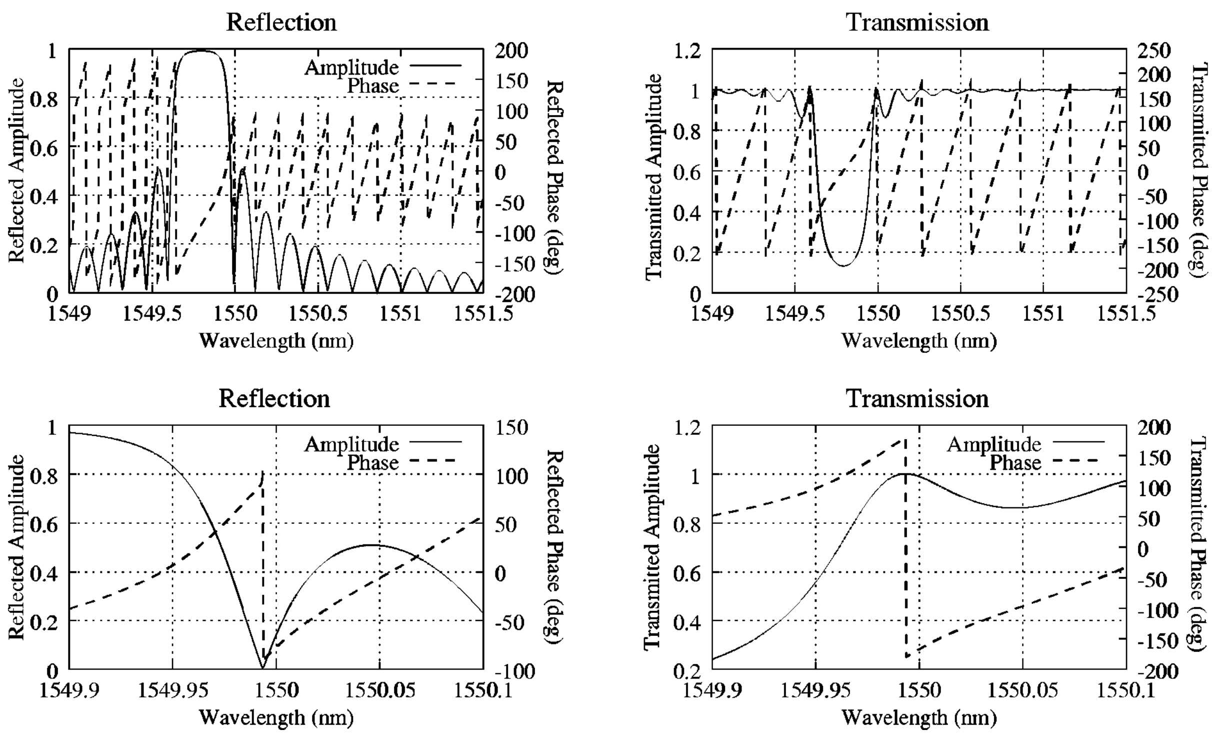

Fig. 8. Reflection and transmission of the Bragg resonator, ignoring any sources of error.

identical to those of Fig. 7, the only differences being placement of PML in both the $+\hat{z}$ and $-\hat{z}$ directions, more cells in the $\hat{z}$ direction to accommodate the geometry shown in Fig. 6, and removal of the electric wall source.

A. Reflected and Transmitted Fields

To obtain the modal reflection and transmission coefficients for the Bragg section at each simulated wavelength, consider Fig. 6 with $\theta = \pi$ rad at $\lambda_0 = 1550$ nm. To compute modal reflection, scattered fields are stored in the xy plane at $z = 0$. A FFT is applied to obtain the fundamental frequency component, and the complex envelope (A_0) of the mode is computed with Eq. (15). Since the incident mode has unit amplitude and zero phase at the origin, $R_0 = A_0$ is the modal reflection coefficient at $z = 0$. The reflection at plane **A** in Fig. 6 is then given as $R_A = A_0 \exp[j\beta_z(l_t - l_s)]$. To obtain the transmission coefficient, scattered fields are stored at $z = 120$ nm, yielding the complex modal envelope A_{120}. Addition of the incident mode at $z = 120$ nm gives the transmission coefficient from 0 to 120 nm, or $T_{0,120} = A_{120} + \exp(-j\beta_z l_t)$. The transmission coefficient from plane **A** to plane **B** is then given as $T_{A,B} = T_{0,120} \exp[j\beta_z(l_t - l_s)]$. Since computational investigations have indicated that R_0, $T_{0,120}$, and the propagation constant follow a linear trend versus excitation wavelength, linear interpolation is employed to obtain results at wavelengths between the simulated data points.

For a fixed wavelength, the Bragg response is computed with 1D transmission-line analysis.[26] The values of R_0 and $T_{0,120}$ at the six excitation wavelengths are interpolated, R_A and $T_{A,B}$ are computed, and an S-parameter matrix is formed for the symmetric Bragg section. Next, the *ABCD* matrix for the section is computed ($\mathbf{A}_S$) and the *ABCD* matrix for the complete resonator is $\mathbf{A}_T = \mathbf{A}_S^N$, where N is the number of sections. After converting $\mathbf{A}_T$ back to an S-parameter matrix, S_{11} and S_{21} give the complex modal reflection and transmission coefficients for the complete Bragg resonator. The response for $N = 10^4$ sections is given in Fig. 8.

Table 4. Sources of Error in the Bragg-Resonator Simulation and Approximate Values

Error Source	Fractional Error in β_z	Fractional Error in Mode Shape	Fractional Error in R and T
FD grid truncation	6.1×10^{-8}	1.0×10^{-6}	—
FD grid resolution	-6.5×10^{-5}	$\mathbf{2.0 \times 10^{-3}}$	—
PML reflection (guided mode)	—	—	1.0×10^{-5}
PML reflection (radiated fields)	—	—	1.0×10^{-5}
Finite time step	-1.7×10^{-4}	—	—
Finite resolution in $\hat{z}$	$\mathbf{6.9 \times 1.0^{-4}}$	—	—

B. Error Quantification

Small amounts of error in the single section response may cause more appreciable error in the complete Bragg response. Table 4 lists the primary sources of error and their estimated values. The numbers in boldface in the table represent error values that are most significant: increased mode amplitude due to finite FD grid resolution and an increase in β_z due to finite FDTD resolution in the propagation direction. The effect of these sources of error is discussed below.

1. Error Source: Increased Mode Amplitude

The finite resolution of the FD method leads to a mode amplitude that is too high in the region of the waveguide discontinuity. Since we are applying the scattered-field

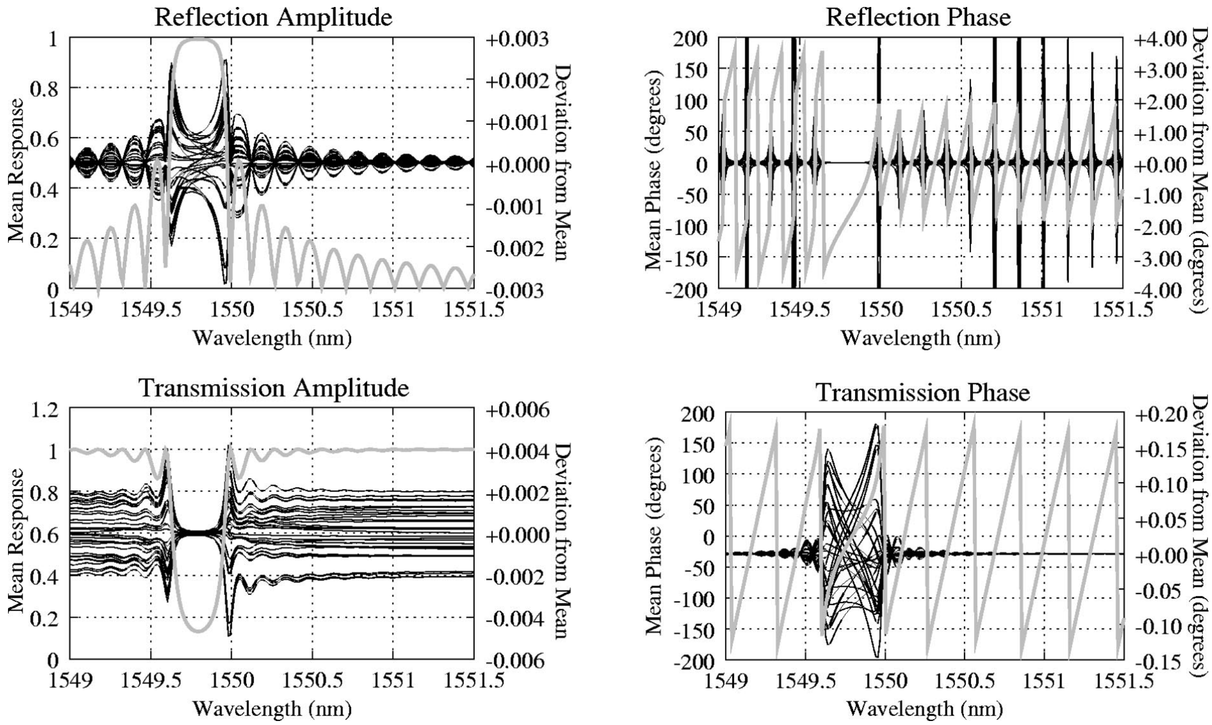

Fig. 9. Transmission and reflection amplitude and phase of the Bragg resonator resulting from random phase shifts on A_0 and A_{120} over 32 realizations. The thick gray curves are the mean and the thin black curves are deviation of the individual realizations from the mean.

formulation and the error is nearly constant over the waveguide discontinuity, the scattered fields will increase linearly with the amount of error. To assess the impact of this effect, we reduced the magnitude of the complex-mode envelopes extracted from the FDTD simulations by 0.2% (as suggested in Table 4) and again plotted the response. The magnitude of fractional change in the reflection and transmission response was less than 2% and 1%, respectively.

2. Error Source: Increase in β_z

The FD-mode solver estimates values for β_z that are too high (~0.07%). At the value of β_z for $\lambda_0 = 1550$ nm, the amount of phase error over the discontinuity length of 120 nm is 0.06°. The resulting error in the phase of A_0 and A_{120} is uncertain owing to the multiple reflections in the discontinuity. However, we may explore the effect of phase error by assuming independent distributions on the phase error for A_0 and A_{120} and produce a number of Monte Carlo realizations. Plotting the response for several random values will provide an indication of the distribution of the error.

For simplicity we assume the phase shift for A_0 and A_{120} to be uniform on [0°, −0.06°]. Figure 9 plots the mean value of transmission and phase of the Bragg resonator along with the response for each of 32 Monte Carlo realizations. The plots show that the most sensitive quantity is the phase of the reflection coefficient near resonances, where reflection is nearly zero. This is reasonable, since we expect numerical difficulty in the computing phase for a small value.

5. CONCLUSION

In this paper we have outlined a method for simulating complex optical devices by applying three basic modeling tools: (1) a 2D FD mode solution technique for finding modes in arbitrary guiding structures, (2) 3D full-wave FDTD analysis of waveguide discontinuities, and (3) network analysis employing a 1D transmission line model. By using the method, we simulated a large (10^4 sections) Bragg resonator. Detailed error analysis indicated that very low error can be obtained for such a problem using this simulation approach. Natural extensions include the simulation of distributed feedback lasers by incorporating gain into the 3D full-wave FDTD simulator.

The authors may be reached at the address on the title page or by e-mail, jensen@ee.byu.edu, and wallacej @ee.byu.edu.

REFERENCES

1. D. Marcuse, "Tilt, offset, and end-separation loss of lowest-order slab waveguide mode," J. Lightwave Technol. **LT-4**, 1647–1650 (1986).
2. S. I. Hosain, J.-P. Meunier, and Z. H. Wang, "Coupling efficiency of butt-jointed planar waveguides with simultaneous tilt and transverse offset," J. Lightwave Technol. **14**, 901–907 (1996).
3. M. D. Feit and J. A. Fleck, "Computation of mode properties in optical fiber waveguides by a propagating beam method," Appl. Opt. **19**, 1154–1164 (1980).
4. W. Huang, C. Xu, S.-T. Chu, and S. K. Chaudhuri, "The finite-difference vector beam propagation method: analysis and assessment," J. Lightwave Technol. **10**, 295–305 (1992).

5. P. Lüsse, P. Stuwe, J. Schüle, and H. Unger, "Analysis of vectorial mode fields in optical waveguides by a new finite difference method," J. Lightwave Technol. **12**, 487–493 (1994).
6. C. L. Xu, W. P. Huang, M. S. Stern, and S. K. Chaudhuri, "Full-vectorial mode calculations by finite difference method," IEE Proc.: Optoelectron. **141**, 281–285 (1994).
7. K. S. Yee, "Numerical solution of initial boundary value problems involving Maxwell's equations in isotropic media," IEEE Trans. Antennas Propag. **AP-14**, 302–307 (1966).
8. A. Taflove and S. C. Hagness, *Computational Electrodynamics: The Finite-Difference Time-Domain Method* (Artech House, Boston, 2000).
9. J.-P. Berenger, "A perfectly matched layer for the absorption of electromagnetic waves," J. Comput. Phys. **114**, 185–200 (1994).
10. H. E. Hernández-Figueroa, F. A. Fernández, and J. B. Davies, "Finite element approach for the modal analysis of open-boundary waveguides," Electron. Lett. **30**, 2031–2032 (1994).
11. J. W. Wallace and M. A. Jensen, "An FD/FDTD method for optical waveguide modeling," in *Proceedings of the 2000 IEEE Antennas and Propagation Society International Symposium* (Institute of Electrical and Electronics Engineers, New York, 2000), Vol. 3, pp. 1380–1383.
12. F. Girardin, G.-H. Duan, and A. Talneau, "Modeling and measurement of spatial-hole-burning applied to amplitude modulated coupling distributed feedback lasers," IEEE J. Quantum Electron. **31**, 834–841 (1995).
13. S. Adachi, "Model dielectric constants of GaP, GaAs, GaSb, InP, InAs, and InSb," Phys. Rev. B **35**, 7454–7463 (1987).
14. D. E. Aspnes and A. A. Studna, "Dielectric functions and optical parameters of Si, Ge, GaP, GaAs, GaSb, InP, InAs, and InSb from 1.5 to 6.0 eV," Phys. Rev. B **27**, 985–1009 (1983).
15. B. Jensen and A. Torabi, "Refractive index of quaternary $In_{1-x}Ga_xAs_yP_{1-y}$ lattice matched to InP," J. Appl. Phys. **54**, 3623–3625 (1983).
16. G. Mur, "Absorbing boundary conditions for the finite-difference approximation of the time-domain electromagnetic-field equations," IEEE Trans. Electromagn. Compat. **EMC-23**, 377–382 (1981).
17. K. K. Mei and J. Fang, "Superabsorption—a method to improve absorbing boundary conditions," IEEE Trans. Antennas Propag. **40**, 1001–1010 (1992).
18. S. D. Gedney, "Anisotropic perfectly matched layer absorbing medium for the truncation of FDTD lattices," IEEE Trans. Antennas Propag. **44**, 1630–1639 (1996).
19. C. M. Rappaport, "Perfectly matched absorbing boundary conditions based on anisotropic lossy mapping of space," IEEE Microwave Guid. Wave Lett. **5**, 90–92 (1995).
20. M. Okoniewski, M. A. Stuchly, M. Mrozowski, and J. DeMoerloose, "Modal PML," IEEE Microwave Guid. Wave Lett. **7**, 33–35 (1997).
21. S. L. Dvorak, "Exact, closed-form expressions for transient fields in homogeneously filled waveguides," IEEE Trans. Microwave Theory Tech. **42**, 2164–2170 (1994).
22. M.-J. Park and S. Nam, "FDTD modal field generation and absorption in homogeneous waveguides with arbitrary cross section," in *Proceedings of the 1996 IEEE Antennas and Propagation Society International Symposium* (Institute of Electrical and Electronics Engineers, New York, 1996), Vol. 2, pp. 1308–1311.
23. C.-N. Kuo, T. Itoh, and B. Houshmand, "Synthesis of absorbing boundary condition with digital filter bank," in *Proceedings of the 1996 IEEE Microwave Theory and Techniques Society International Symposium* (Institute of Electrical and Electronics Engineers, New York, 1996), Vol. 2, pp. 1043–1046.
24. M. Chen, B. Houshmand, and T. Itoh, "FDTD analysis of a metal-strip-loaded dielectric leaky-wave antenna," IEEE Trans. Antennas Propag. **45**, 1294–1301 (1997).
25. M. A. Gribbons, W. P. Pinello, and A. C. Cangellaris, "Stretched coordinate technique for numerical absorption of evanescent and propagating waves in planar waveguiding structures," in *Proceedings of the 1995 IEEE Microwave Theory and Techniques Society International Symposium* (Institute of Electrical and Electronics Engineers, New York, 1995), Vol. 1, pp. 31–34.
26. G. Gonzalez, *Microwave Transistor Amplifiers* (Prentice-Hall, Upper Saddle River, N.J., 1997).